

Joint Research Highlights

Multiband Superconductivity in Strongly Hybridized $1T'$ -WTe₂/NbSe₂ Heterostructure

Inducing superconductivity by proximity in materials with nontrivial band topology has become a method in the search for unconventional forms of superconducting pairing. At the one-dimensional (1D) edges of two-dimensional (2D) topological insulators the presence of non-Abelian parafermions has been predicted, which could have important applications in topological quantum computation. Here, we investigate heterostructures of the quantum spin Hall candidate $1T'$ -WTe₂, grown by *in situ* van der Waals epitaxy on a superconductor 2H-NbSe₂ by scanning tunneling spectroscopy down to 500 mK, which enables us to resolve the superconducting local density of states (LDOS) across the interface between the two materials.

Figure 1 shows scanning tunneling microscopy (STM) data of $1T'$ -WTe₂/2H-NbSe₂ heterostructures. In agreement with previous studies of WTe₂ on bilayer graphene, we observe islands with disordered boundaries and sizes up to a few tens of nanometer in diameter that are polycrystalline on NbSe₂ substrates. Lattice parameters estimated from FFT patterns of the STM images are $a \sim a_1 = 3.5 \pm 0.2 \text{ \AA}$, and $b \sim 2a_2 \cos(30^\circ) = 6.2 \pm 0.3 \text{ \AA}$, in good agreement with the lattice parameters of WTe₂ ($a = 3.48 \text{ \AA}$ and $b = 6.28 \text{ \AA}$) and NbSe₂ ($a_1 = a_2 = 3.45 \text{ \AA}$). Local lattice matching implies a 5% compressive lattice strain along b , which has previously been shown to further stabilize the WTe₂ bulk gap.

In Fig. 2, tunneling spectra taken on the monolayer WTe₂ and the NbSe₂ substrate at 500 mK are presented, demonstrating the clear signature of a superconducting energy gap in the 2D monolayer WTe₂. The measured superconducting LDOS within a self-consistent multiband framework that considers a superconducting gap of each band and an inter-band Cooper-pair tunneling rate. It has been already known

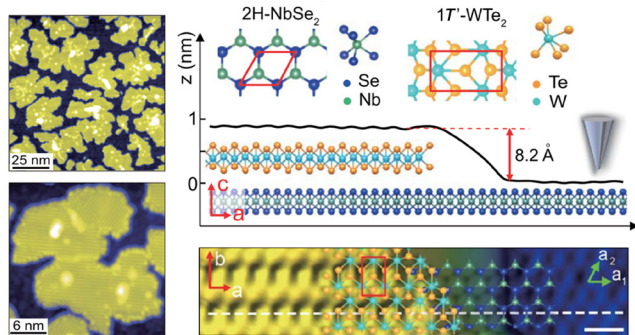


Fig. 1. (left panels) STM topography of monolayer $1T'$ -WTe₂ islands grown on a single crystal of 2H-NbSe₂ by van der Waals epitaxy. Upper right panel shows height profile corresponding to the dashed white line in the lower right panel, showing a monolayer height of 8.2 Å. The inset shows the respective $1T'$ -WTe₂ and 2H-NbSe₂ crystal structures. Atomic-resolution close-up of the $1T'$ -WTe₂ edge, showing detail of the atomic alignment.

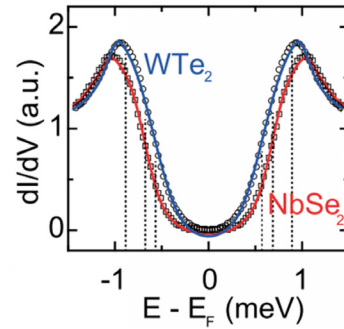


Fig. 2. tunneling spectra comparing the WTe₂/NbSe₂ spectrum with that measured on the bare NbSe₂ substrate. Solid red and blue lines are fits to our two-band (NbSe₂) and three-band (WTe₂) models, respectively.

that the gap of NbSe₂ is well described with a scheme of intrinsic two-band superconductor, and here we consider a third order parameter Δ_{WTe_2} , coupled to the two NbSe₂ bands, assuming intrinsic $\Delta_{WTe_2} = 0$. Fits to both a two-band (NbSe₂, red line) and a three-band (WTe₂/NbSe₂, blue line) model explain the data well (Fig. 2) and reproduce the known NbSe₂ order parameters. Self-consistently obtained $\Delta_{WTe_2} = (0.57 \pm 0.02) \text{ meV}$, reflecting induced pairing, which suggests strong hybridization between the overlayer and substrate.

Our tight-binding calculations revealed that the strong hybridization in WTe₂/NbSe₂ heterostructure substantially weakens the topological edge state signature compared with WTe₂/HOPG, which is only weakly hybridized. In spite of

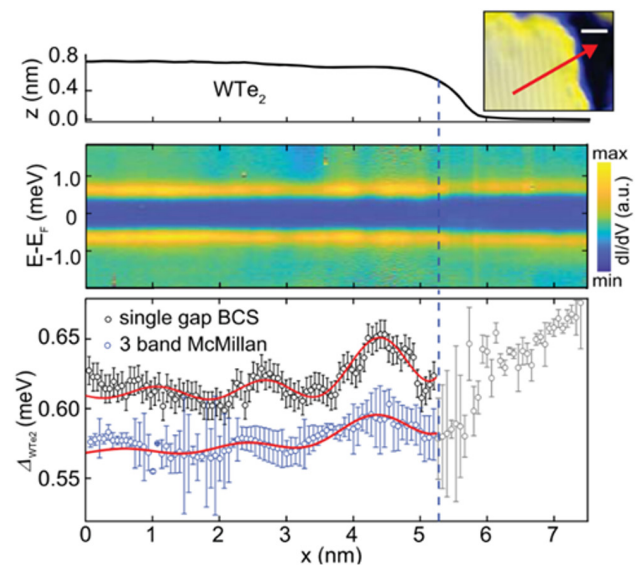


Fig. 3. (upper panel) STM-height profile measured across a clean edge of a WTe₂ monolayer crystal. The inset shows the corresponding STM topograph indicating position and direction of the line profile (red arrow). (middle) A series of tunneling spectra measured $T = 500 \text{ mK}$ for points across the edge. (lower) Extracted spatial profile of the induced order parameter $\Delta_{WTe_2}(x)$ (blue), compared with a single-band BCS-Dynes model (black).

the suppressed edge states, however, we observed enhanced order parameter at the edge as shown in Fig. 3, where a spatial profile of the extracted order parameter $\Delta_{\text{WTe}_2}(x)$ based on the three-band superconductivity analysis is shown. The plot also shows spatial oscillations with a period of ~ 2 nm. Oscillations of comparable period are also observed in the order parameter extracted from a simple single-band BCS model. This suggests that these arise from Friedel-like oscillations in the local density of states due to scattering of 2D bulk states at the WTe_2 edge. The exponential decaying 1D edge state, with decay length (1.1 ± 0.2) nm is comparable to the normal-state LDOS of the edge.

Reference

[1] W. Tao *et al.*, Phys. Rev. B **105**, 094512 (2022).

Authors

W. Tao^a, Z. J. Tong^a, A. Das^b, D.-Q. Ho^a, Y. Sato, M. Haze, J. Jia^a, Y. Que^a, F. Bussolotti^c, K. E. J. Goh^{a,c}, B. Wang^d, H. Lin^e, A. Bansil^d, S. Mukherjee^b, Y. Hasegawa, and B. Weber^{a,f}

^aNanyang Technological University, Singapore

^bIndian Institute of Technology Madras

^cAgency for Science Technology and Research (A*STAR)

^dNortheastern University

^eInstitute of Physics, Academia Sinica

^fMonash University

PI of Joint-use project: B. Weber

Host lab: Hasegawa Group

Bayesian Optimization of Thin Film Growth Parameters

The use of thin films for developing new crystalline materials is an attractive approach because the crystal growth process is fast, the volume of required material is small, and a relatively large number of samples with varying composition or structure can be rapidly synthesized. However, the physical properties of thin films are very sensitive to small changes in the various process parameters that control the film growth. Besides the usual thermodynamic parameters, such as pressures or temperatures, thin film growth is also affected by kinetic effects, such as the growth rate. For this reason, the process space, in addition to the composition space, can be very multi-dimensional. Exhaustive mapping of materials properties over the whole available temperature, pressure, growth rate, etc. ranges is therefore very time consuming and in practice, a human operator would struggle in determining the optimum combination of parameter combinations to test to complete a materials exploration or optimization task with the smallest number of experiments. In this regard, help may be available from the various machine learning methods that have been developed in recent years. In particular, the dimensionality problem of the process parameter space can be handled by Bayesian optimization, as illustrated in Fig. 1.

The thin film synthesis system illustrated in Fig. 1 was recently developed by Dr. Ohkubo at NIMS [1]. Nitride thin films are grown by metal-organic molecular beam epitaxy (MO-MBE) from an organic precursor in the presence of activated nitrogen plasma. In this work, the growth of TiN was attempted as a demonstration of the MO-MBE process using tetrakis(dimethylamido)titanium (TDMAT) as a Ti source. The TiN films were characterized by x-ray diffraction (XRD) and transport analysis. In particular, the superconducting transition temperature of TiN was used as a more sensitive measure of the crystalline quality of the films than

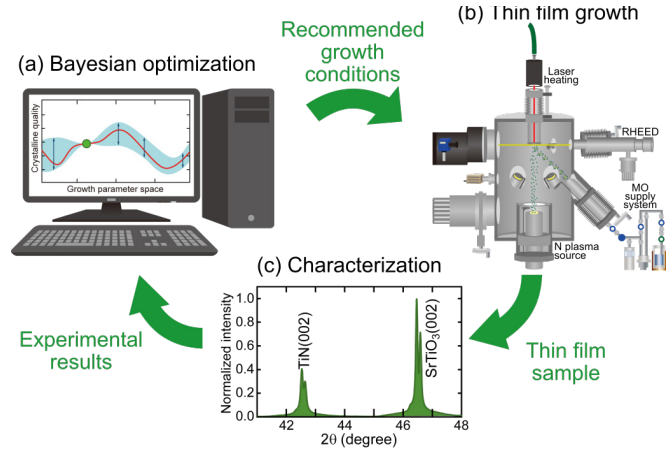


Fig. 1. Closed-loop optimization of epitaxial thin film growth conditions using a Bayesian approach. Nitride thin films were grown by metal-organic molecular beam epitaxy (b) and characterized by x-ray diffraction (c). The film peak intensity was used as the feedback for the Bayesian optimizer (a).

is possible by XRD analysis. A small set of initial samples was synthesized by manually selecting the primary process parameters: the film growth temperature, the TDMAT source foreline pressure, the nitrogen flow rate, and the excitation power of the nitrogen plasma source. These four parameters effectively determine the growth mode (temperature), rate (TDMAT flow rate), and the nitrogen activity.

After the initial set of samples were synthesized and characterized by XRD, further combinations of the four main parameters were selected by a Bayesian optimization process using the normalized TiN peak intensity in the XRD pattern as the objective function. The growth temperature range was limited to 550 to 900 °C, the TDMAT pressure was between 0.5 and 10.5 Torr, the N_2 flow rate was limited to 0.5 to 5 sccm, and the plasma source power limits were 270 to 500 W, forming a search grid of $7 \times 100 \times 45 \times 23$ points. After every film growth experiment, the XRD pattern was analyzed and a new process point was determined by the Bayesian process. The cycle was repeated for 20 times. No further improvement of the XRD peak intensity was obtained after 10 cycles.

The low-temperature superconducting transition temperature measurements were done at ISSP. The gradual improvement of the critical temperature in the Bayesian optimization process is shown in Fig. 2. It can be seen that the maximum T_c of 5.2 K was obtained on the tenth cycle, after which no further increase was obtained.

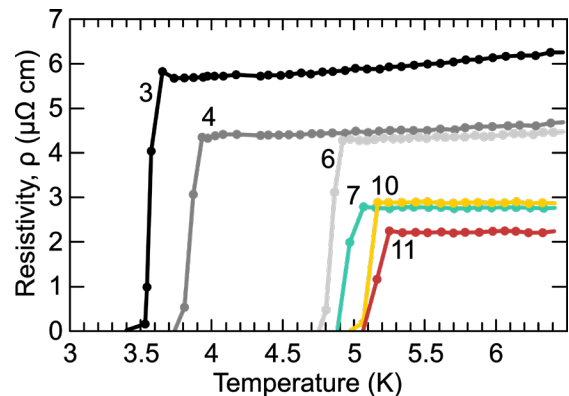


Fig. 2. Gradual improvement of the superconducting transition temperature of TiN thin films as a function of the synthesis-characterization-selection cycle index. No further improvement was obtained after just 10 synthesis experiments.

This experiment was the first demonstration of closed-loop thin film synthesis controlled by a machine learning algorithm for reducing the number of film growth experiments required to reach the optimal physical properties. In this work, XRD was used as the source of the feedback signal for the Bayesian process. This means that the cycle time (Fig. 1) was limited by the diffraction analysis, not by synthesis. In addition to the XRD and transport data, in situ electron diffraction data was also collected. In the future, it may be possible to greatly increase the rate of materials development by using real-time in situ characterization tools for providing the feedback signal for a Bayesian process optimizer.

Reference

[1] I. Ohkubo, Z. Hou, J. N. Lee, T. Aizawa, M. Lippmaa, T. Chikyow, K. Tsuda, and T. Mori, *Mater. Today Phys.* **16**, 100296 (2021).

Authors

I. Ohkubo^a, Z. Hou^a, J. N. Lee, T. Aizawa^a, M. Lippmaa, T. Chikyow^a, K. Tsuda^a, and T. Mori^a
^aNIMS

PI of Joint-use project: I. Ohkubo
 Host lab: Lippmaa Group

Adsorption and Reaction of Formic Acid on Cu(111)

Hydrogen is one of the promising energy sources toward the carbon neutral and sustainable society. Formic acid (HCOOH) has attracted attention as a candidate for the hydrogen storage material because it is nontoxic and exists as a stable molecule at standard temperature and pressure conditions. In general, HCOOH can be catalytically converted into CO₂ and H₂ via dehydrogenation or into CO and H₂O via dehydration. Among others, a Cu surface is one of the attractive catalysts, because HCOOH is selectively decomposed into CO₂ and H₂ via the formate (HCOO) intermediate without generating CO. However, the mechanism of HCOOH dehydrogenation is not yet fully understood. One of the reasons may be that the state of HCOOH on a Cu surface, in which HCOOH is adsorbed in a polymeric form, is not yet determined. Furthermore, there is a discrepancy between the computational and experimental adsorption energies [1]. Toward the full understanding of the HCOOH dehydrogenation on Cu catalyst, we conducted density functional theory studies on monomeric as well as polymeric adsorption of HCOOH on Cu(111), as well as their dehydrogenation reactions.

We used the rev-vdW-DF2 [2], a variant of the van der Waals density functional (vdW-DF). Use of vdW-DF is essential, as the interaction between HCOOH and Cu surface is very weak and is of dispersion type. The surfaces were represented using slab models, and the electrostatic interaction in the surface normal direction was treated rigorously by using the effective screening medium method.

We first investigated the monomeric adsorption of HCOOH on Cu(111) and found that the adsorption energy is much smaller than the experimental value, when the generalized gradient approximation is used, while it is in better agreement with the experiment, when the dispersion forces are properly described via vdW-DF [3].

We then investigated the molecular structures for the polymeric HCOOH adsorption. In the literature, there

have been proposals of the so-called α - and β -polymeric structures on the surfaces (Fig. 1), according to the crystalline HCOOH, but the stable form on Cu(111) has yet to be resolved. We explored the stable structure of polymeric HCOOH by considering various structures and in-plane periodicities. HCOOH interacts weakly with the surface, while it interacts with the neighboring molecules via the H-bonding-like interaction. We found that the β -polymeric form is energetically more stable than the α one, although they are energetically competing. However, by simulating the vibrational spectra, scanning tunneling microscopy/atomic force microscopy (AFM) images (Fig. 2), and by comparing with the experiments, we concluded that α -polymeric HCOOH is more plausible and has been formed and observed in the experiments [4, 5]. We then studied the dehydrogenation reaction by taking the edge effect into account. We found that the dehydrogenation reaction is facilitated at the edge of the polymeric HCOOH chain, and it barely occurs within the polymeric HCOOH chain. Our results are consistent with the previous experiments.

The polymeric HCOOH is decomposed (in part) into HCOO and form complex nanostructures, depending on the annealing temperature. We performed extensive structure search of HCOOH-HCOO and HCOO with different compositions and successfully determined the structures of chain-like monodentate HCOO + HCOOH and monodentate HCOO + bidentate HCOO aggregates as well as bidentate HCOO clusters by evaluating the adsorption energies and simulating the AFM images [4].

In summary, we have clarified the adsorption states of HCOOH as well as the aggregates composed of HCOOH and HCOO and the mechanism of the dehydrogenation of HCOOH into HCOO on Cu(111), and succeeded in tracking the fate of HCOOH on Cu(111) upon annealing.

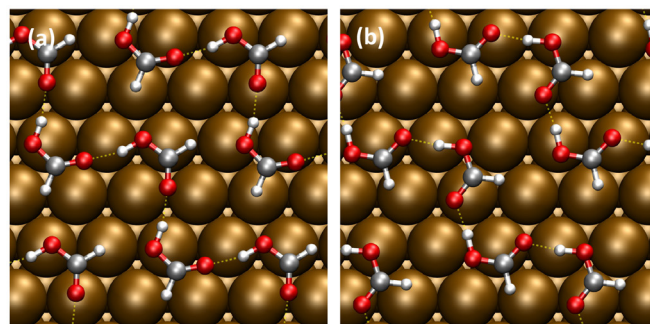


Fig. 1. Structures of (a) α -polymeric and (b) β -polymeric HCOOH's on Cu(111).

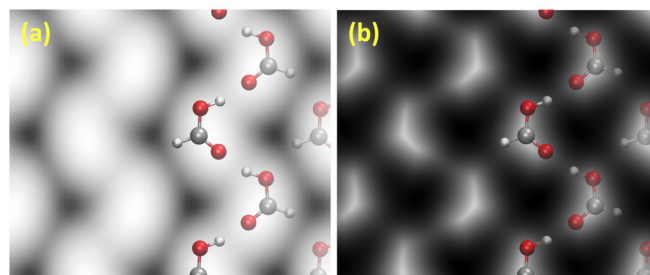


Fig. 2. (a) Simulated scanning tunneling microscopy image and (b) simulated atomic force microscopy image of polymeric HCOOH in the α -form on Cu(111). Tersoff-Hamann and probe particle methods were used to generate the former and the latter, respectively.

References

- [1] Y. Shiozawa, T. Koitaya, K. Mukai, S. Yoshimoto, and J. Yoshinobu, *J. Chem. Phys.* **143**, 234707 (2015).
 [2] I. Hamada, *Phys. Rev. B* **89**, 121103(R) (2014).
 [3] S. E. M. Putra, F. Muttaqien, Y. Hamamoto, K. Inagaki, I. Hamada, and Y. Morikawa, *J. Chem. Phys.* **150**, 154707 (2019).
 [4] A. Shiotari*, S. E. M. Putra*, Y. Shiozawa, Y. Hamamoto, K. Inagaki, Y. Morikawa, Y. Sugimoto, J. Yoshinobu, and I. Hamada, *Small* **17**, 2008010 (2021). (*: equal contribution)
 [5] S. E. M. Putra, F. Muttaqien, Y. Hamamoto, K. Inagaki, A. Shiotari, J. Yoshinobu, Y. Morikawa, and I. Hamada, *Phys. Rev. Materials* **5**, 075801 (2021).

Authors

I. Hamada^a, S. E. M. Putra^a, F. Muttaqien^b, Y. Hamamoto^a, K. Inagaki^a, A. Shiotari^c, Y. Sugimoto^c, J. Yoshinobu, and Y. Morikawa^a

^aOsaka University

^bInstitut Teknologi Bandung

^cThe University of Tokyo

PI of Joint-use project: I. Hamada

Host lab: Yoshinobu Group

Photon Echo from Lensing of Fractional Excitations in Tomonaga-Luttinger Spin Liquid

Physicists routinely diagnose the properties of a material by its linear responses to external stimuli. The recently developed nonlinear spectroscopy measures nonlinear optical responses to obtain more information on the material. Yet, it is often unclear if there is a straightforward connection between such nonlinear responses and the material's properties, especially when its constituent particles strongly interact with one another. We addressed this question by studying theoretically a prototypical strongly interacting system, the Tomonaga-Luttinger spin liquid. Tomonaga was the first to point out that the low-energy excitations of fermions in one dimensions can be described in terms of quantized sound waves (phonons). Subsequent studies have established that the quantum theory of sound waves, which is now called Tomonaga-Luttinger liquid, can describe the universal low-energy physics of a wide variety of one-dimensional critical quantum many-body systems. This includes critical one-dimensional quantum spin systems, which are regarded as Tomonaga-Luttinger spin liquids.

A remarkable feature of the Tomonaga-Luttinger spin liquids is “fractionalization” of the spin excitations. In

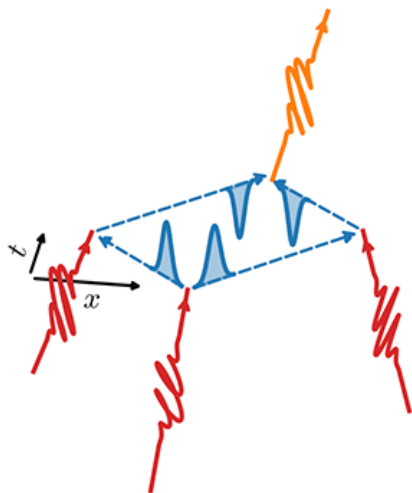


Fig. 1. Schematic diagram of the photon echo. The first photon creates a pair of fractionalized spinon excitations, the second and third photons reflect them back, refocusing them to give rise to a sharp echo.

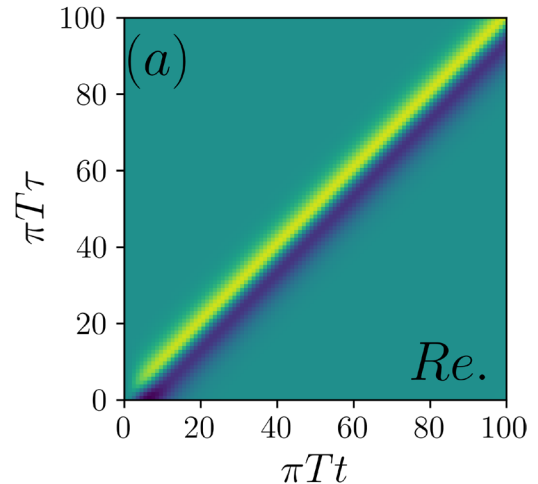


Fig. 2. The photon echo signal in real time. Despite the fractionalization, the sharp signal remains over a long period of time thanks to the spinon lensing effect.

ordered magnets, the elementary excitation corresponds to a single spin flip and called “magnon”. A single magnon is created by an absorption of photon (or a scattering of neutron), resulting in a sharp peak in the spectrum of linear response. In contrast, in the Tomonaga-Luttinger spin liquid, the single spin flip caused by an absorption of photon fractionalizes into two “spinon” excitations. This leads to a continuum in the linear response spectrum. While this “two-spinon continuum” is a characteristic signature of the fractionalization, the absence of the sharp peak makes the analysis difficult.

We analyzed nonlinear optical responses of the Tomonaga-Luttinger spin liquids in the context of terahertz (THz) two-dimensional coherent spectroscopy (2DCS), which is developing rapidly in recent years. We find a direct link between a specific nonlinear response, known as photon echo, and the dynamical properties of the excitations in this system.

The central finding in our work was that we can recover the sharp peak even in the Tomonaga-Luttinger spin liquid with the fractionalized spinon excitations, if we look at the nonlinear responses in a particular manner. The photon echo is measured by three successive optical pulses. The sharp response appears as a surge in the response after the last pulse. In the Tomonaga-Luttinger spin liquid, we trace the origin of the photon echo to a unique “lensing” phenomenon: The first pulse creates a pair of spinons moving in opposite directions. The second and third pulses change their directions of motion. These two excitations thus come back toward each other and reunite, thereby giving rise to the echo. Dissipation and dispersion effects, which suppress the lensing phenomenon, are sensitively picked up by the echo signal. This will make the 2DCS a very useful experimental probe to study these effects, which would be quite difficult with conventional experimental measurements.

Our work thus uncovers one aspect of the many uses of the nonlinear spectroscopy and related dynamical phenomena. We believe that more interesting physics is yet to be explored in the nonlinear responses of strongly correlated systems, and hope that our work will stimulate further theoretical and experimental studies.

Reference

- [1] Z.-L. Li, M. Oshikawa, and Y. Wan, *Phys. Rev. X* **11**, 031035 (2021).

Authors

Z.-L. Li^a, M. Oshikawa, and Y. Wan^a

^aInstitute of Physics, Chinese Academy of Sciences

PI of Joint-use project: Y. Wan

Host lab: Oshikawa Group

Pressure-Induced Multicriticality and Electronic Instability in the Quasi-Kagome Ferromagnet URhSn

URhSn crystallizes in the hexagonal ZrNiAl-type structure without inversion symmetry. The U atom forms the quasi-kagome structure, in which the magnetic frustration is potentially expected. The rare-earth based family, such as CePdAl and YbAgGe, indeed shows the novel magnetic phase diagram due to this magnetic frustration. In U based system, the ferromagnetic quantum critical behavior is well established, for example in UCoAl and URhAl, where the wing-shaped temperature-pressure-field phase diagram associated with the first order metamagnetic transition is demonstrated.

In URhSn, two successive transitions had been reported in the previous literature. The one is the ferromagnetic Curie temperature at $T_C = 16$ K with the relatively large ordered moment of $2.1 \mu_B$ directed along c-axis, the other transition occurs at $T_O = 54$ K with the large specific heat jump. The origin for the latter transition is still unclear from the neutron scattering experiments and Mossbauer spectroscopy, meaning that the order parameter remains “hidden”. Thus a quadrupole or multipole order is inferred [1].

In this study, we performed the electrical resistivity measurements under pressure up to 11 GPa [2]. The two transitions are abruptly switched to the two different transitions at the critical pressure, $P_C \sim 6.3$ GPa, indicating two bicritical points associated with the Fermi surface reconstructions.

High quality single crystals were grown using the Czochralski method in a tetra-arc furnace. The obtained single crystals were then annealed at 800 °C under vacuum for one month. The residual resistivity ratio (RRR) is about 40, and the de Haas-van Alphen oscillations are successfully detected, revealing the mean free path of ~ 1000 Å, indicating the high quality of our sample. A bar shaped single crystal was set into a cubic anvil cell for the resistivity measurements at high pressure up to 11 GPa and at low temperatures down to 2.5 K. The electrical current was applied along the [11-20] direction.

Figure 1 shows the temperature-pressure phase diagram determined from the resistivity measurements. Two transitions at T_C and T_O were clearly detected with two kinks in the resistivity measurements. Interestingly, T_O decreases with pressure, while T_C slightly increases up to the critical pressure, $P_C \sim 6.3$ GPa. Further increasing pressure, T_O increases, displaying a sharp minimum at P_C as a function of pressure, while T_C drops suddenly, and increases again. These abrupt changes of T_C and T_O indicate that the first order phase boundary exists at P_C , shown at the ABC line in the phase diagram of Fig. 1. The residual resistivity also abruptly increases at P_C and remains the large value, suggesting the drastic change of the electronic state. The resistivity A coefficient, assuming the T^2 dependence of the resistivity, also shows a sudden increase above P_C , which also supports the drastic change of the electronic state,

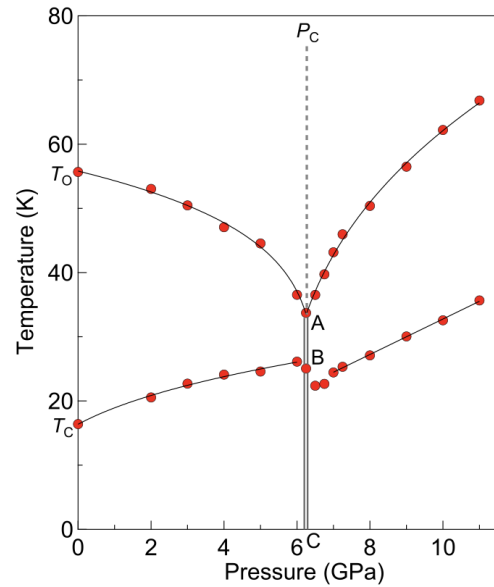


Fig. 1. Temperature-pressure phase diagram of URhSn.

possibly associated with the Fermi surface reconstruction.

Of course, we don't know yet what are the order parameters for the different two phases above P_C . The present results, however, reveals the novel pressure-induced quantum phase transitions. Interestingly, this multicriticality is possibly related to the higher order multiple order and the associated multiple phases, which occurs in the $5f$ -electron systems without inversion symmetry in the crystal structure. Further experiments with microscopic probes are required.

References

- [1] Y. Shimizu, A. Miyake, A. Maurya, F. Honda, A. Nakamura, Y. J. Sato, D. Li, Y. Homma, M. Yokoyama, Y. Tokunaga, M. Tokunaga, and D. Aoki, Phys. Rev. B. **102**, 134411 (2020).
- [2] A. Maurya, D. Bhoi, F. Honda, Y. Shimizu, A. Nakamura, Y. J. Sato, D. Li, Y. Homma, M. Sathiskumar, J. Gouchi, Y. Uwatoko, and D. Aoki, Phys. Rev. B **104**, 195119 (2021).

Authors

D. Aoki^a and A. Maurya^a

^aIMR, Tohoku University

PI of Joint-use project: A. Maurya

Host lab: Uwatoko Group

Pressure-Induced Lifshitz Transition Observed from Nuclear Magnetic Resonance in S-Substituted FeSe

We performed ^{77}Se -nuclear magnetic resonance (NMR) measurements under pressures of up to 3.9 GPa on 12 % S-substituted FeSe and observed a pressure-induced Lifshitz transition at around 1.0 GPa from the Knight shift (K) and relaxation rate ($1/T_1$) [1].

FeSe is unique among iron-based superconductors in the point that small unconnected Fermi surfaces induce superconductivity without magnetism. The left panel of Fig. 1(a) shows the Fermi surfaces in the tetragonal phase. The Fermi surfaces consist of the small hole pockets at point Γ , $k = (0, 0)$, and anisotropic electron pockets at point X , $k = (\pi, 0)$ or $(0, \pi)$ [2-4]. The superconductivity appears in the nematic phase where four-fold rotational

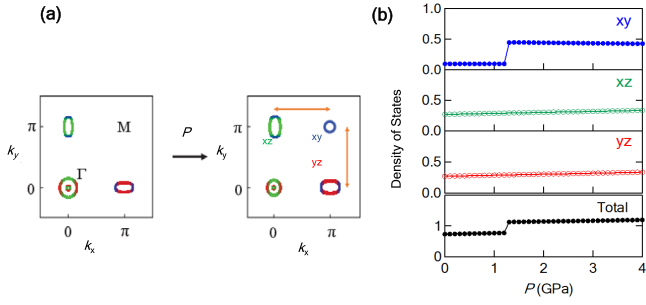


Fig. 1. (a) Schematic Fermi surfaces of pure FeSe in a tetragonal phase theoretically derived at ambient pressure and high pressure. The Fermi surfaces colored in green, red, and blue represent d_{xz} , d_{yz} , and d_{xy} orbitals, respectively. Arrows indicate the nesting of d_{xy} orbitals between points M and X. (b) The density of states (DOS) originating from each orbital and the total DOS calculated theoretically for 10% S-substituted FeSe.

symmetry is broken. Unlike iron-based pnictides, this orbital configuration reduces the likelihood of nesting between electron and hole pockets with the same orbital, leading to the absence of magnetism.

Upon pressure application, FeSe undergoes an antiferromagnetic (AF) order instead of the nematic order [5]. Although the nematic and AF phases are complicatedly entangled in the pressure versus temperature (P - T) phase diagram, S substitution makes possible to resolve the complex overlap between them [6].

Figure 2(a) shows the P - T phase diagram for 12% S-substituted FeSe determined from ac susceptibility and ^{77}Se -NMR measurements [1]. A single crystal with dimensions of approximately $1.0\text{mm} \times 1.0\text{mm} \times 0.5\text{mm}$ was used for these experiments. Figure 2(b) shows $1/T_1T$ for the field parallel to the FeSe plane. The color plot in Fig. 2(a) obtained from $1/T_1T$ provides a measure of low-energy spin fluctuations. As seen from the color plot, AF fluctuations below and above 1 GPa are of different origins. Strong AF fluctuations develop without magnetism in the nematic phase below 1 GPa, whereas AF fluctuations seem to be weak above 1 GPa despite of the AF-phase boundary.

The anomaly at 1 GPa is also observed in the shift K . The NMR spectra at 60 K and K at 60 and 70 K are shown in Fig. 3(a) and 3(b), respectively. The shift is decomposed as $K = K_{\text{orb}} + K_{\text{spin}}$ where K_{spin} and K_{orb} represent the spin and orbital parts, respectively. The former and latter are T -dependent and T -independent, respectively. The orbital part K_{orb} is

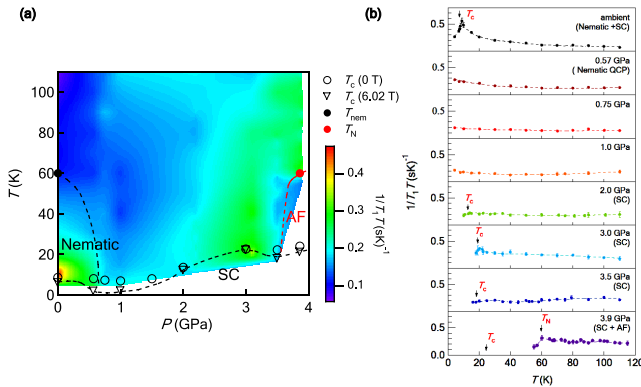


Fig. 2. (a) Color plot of relaxation rate divided by temperature ($1/T_1T$). The superconducting (SC) phase shows a double-dome structure at 6.02 T. T_C s shown by circles and inverted triangles are determined from AC susceptibility measurements at 0 T and 6.02 T, respectively. Both nematic and SC orders are absent at 1.0 GPa at 6.02 T. (b) T dependence of $1/T_1T$ measured at 6.02 T for the field parallel to the FeSe plane. T_C s shown by arrows are the same with those in Fig. 2(a).

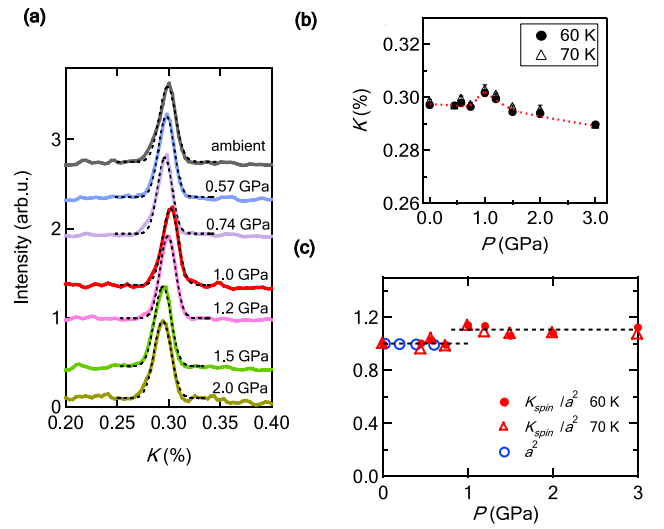


Fig. 3. (a) Pressure dependence of the NMR spectra at 60 K. Each spectrum is fitted with a Gaussian function, as indicated by dotted curves. (b) Pressure dependence of the Knight shift (K) measured at 60 and 70 K. The dotted curves are guides to the eye. (c) Pressure dependence of the spin part of K divided by a^2 (K_{spin}/a^2) where a represents the square of the a -axis lattice constant. In the figure, K_{spin}/a^2 and a^2 are normalized by those at ambient pressure. The dashed lines represent the average of K_{spin}/a^2 at pressure regions below and above 1 GPa. The results in Fig. 3(c) are comparable to theoretical calculations in Fig. 1(b).

$\sim 0.26\%$ at low pressures below 1 GPa and decreases 0.005 and 0.01 % at 2 and 3 GPa, respectively. The decrease at high pressures is estimated from the decrease in K_{spin} due to superconductivity [1]. The spin part K_{spin} and the uniform susceptibility $\chi(0)$ are related to $K_{\text{spin}} = A\chi(0)$ where A is the hyperfine coupling. Since $\chi(0)$ can be described using the density of states (DOS) of a 2D free electron system, K_{spin} is expressed as $K_{\text{spin}} \propto (Na)^2m/\hbar$ where N^2 , a , and m are the total number of lattices, lattice constant, and electron mass, respectively. Two quantities, K_{spin}/a^2 and a^2 , normalized by those at ambient pressure are shown in Fig. 3(c).

The step-like enhancement of K_{spin}/a^2 at 1 GPa implies the appearance of other Fermi surfaces, as expected theoretically at high pressures [4] (See the right panel of Fig. 1(a)). The results of K_{spin}/a^2 are comparable to the theoretically calculated total DOS shown in Fig. 1(b). The Fermi surface at point M, $\mathbf{k} = (\pi, \pi)$, is of d_{xy} -orbital origin, leading to the nesting with unconnected Fermi surfaces with the same d_{xy} orbital (See yellow arrows in Fig. 1(a)). In fact, the enhancement of K_{spin}/a^2 seems to be smaller than that shown in Fig. 1(b), implying that the size of the hole pocket at the point M is fairly small. This unbalanced nesting would induce very weak AF fluctuations observed at high pressures above 1 GPa.

In conclusion, we performed ^{77}Se -NMR measurements on 12% S-substituted FeSe under pressures of up to 3.9 GPa. We observed the anomalies of K and $1/T_1T$ corresponding to the theoretically predicted Lifshitz transition. Our results suggest that the emergence of the d_{xy} orbital and its orbital-selective coupling play a key role to understand the electronic properties of FeSe at high pressures.

References

- [1] T. Kuwayama, *et al.*, Scientific Reports **11**, 17265 (2021).
- [2] M. D. Watson, *et al.*, Phys. Rev. B **91**, 155106 (2015).
- [3] L. Fanfarillo, *et al.*, Phys. Rev. B **97**, 121109 (2018).
- [4] Y. Yamakawa, *et al.*, Phys. Rev. B **96**, 144509 (2017).
- [5] J. P. Sun, *et al.*, Nat. Commun. **7**, 12146 (2016).
- [6] K. Matsuura, *et al.*, Nat. Commun. **8**, 1143 (2017).

Authors

T. Kuwayama^a, K. Matsuura^b, J. Gouchi, Y. Yamakawa^c, Y. Mizukami^b, S. Kasahara^a, Y. Matsuda^a, T. Shibauchi^b, H. Kontani^c, Y. Uwatoko, and N. Fujiwara^a
^aKyoto University
^bUniversity of Tokyo
^cNagoya University

PI of Joint-use project: N. Fujiwara
 Host lab: Uwatoko Group

High-Pressure Phase Diagrams of FeSe_{1-x}Te_x: Correlation Between Suppressed Nematicity and Enhanced Superconductivity

The interplay among magnetism, electronic nematicity, and superconductivity is the key issue in strongly correlated materials including iron-based, cuprate, and heavy-fermion superconductors. Magnetic fluctuations have been widely discussed as a pairing mechanism of unconventional superconductivity, but recent theory predicts that quantum fluctuations of nematic order may also promote high-temperature superconductivity. This mechanism of unconventional superconductivity is distinctly different from the one based on spin fluctuations, and its experimental verification remains elusive. This is partly due to the closeness between nematic and antiferromagnetic orders in iron-pnictide superconductors, and the enhanced superconductivity can be found near both ends of these two ordered phases, where both magnetic and nematic fluctuations are enhanced. FeSe with a superconducting transition temperature $T_c \approx 9$ K serves as an ideal platform to study the relationship between the nematicity and superconductivity, because unlike other iron-based superconductors its nematic order below the structural transition at $T_s \approx 90$ K is accompanied by no magnetic order [1].

In this study, we have succeeded in growing high-quality single crystals of FeSe_{1-x}Te_x superconductors, another family of FeSe-based materials, which we use to study the electronic phase diagram in a wide range of Te composition under pressure [2]. The single crystals of FeSe_{1-x}Te_x were grown by the chemical vapor transport technique, which overcomes the phase separation issue reported in the previous crystal growth for a low Te composition range. The resistivity and synchrotron X-ray diffraction measurements show that the electronic nematic transition

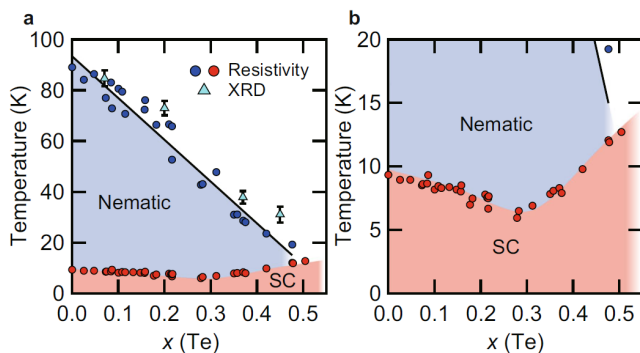


Fig. 1. a, Nematic and superconducting transition temperatures as a function of Te composition $x(\text{Te})$. The blue and red circles represent the nematic (T_s) and superconducting (T_c) transition temperatures, respectively, determined by the resistivity measurements. The light blue triangles represent T_s , determined by the splitting of the Bragg peaks in the XRD measurements. b, The same as in a, but the temperature range is 0–20 K.

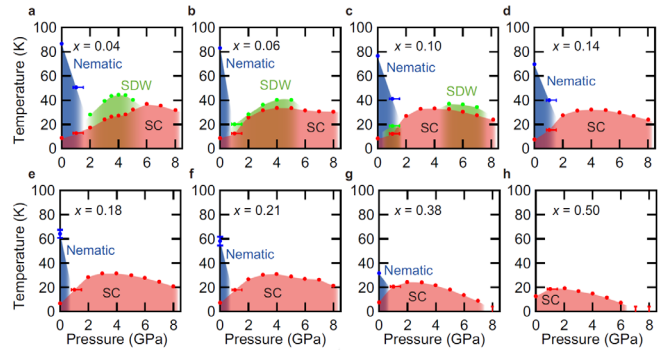


Fig. 2. Pressure dependence of T_c , T_s , and T_m indicated by red, blue, and green circles, respectively, for $x(\text{Te}) \approx 0.04$ (a), 0.06 (b), 0.10 (c), 0.14 (d), 0.18 (e), 0.21 (f), 0.38 (g), and 0.50 (h).

temperature T_s is monotonically suppressed with increasing Te composition. As shown in Fig. 1, the nematic transition can be completely suppressed by $\sim 50\%$ substitution, while the superconducting transition temperature T_c shows a nonmonotonic composition dependence. We find that this nonmonotonic dependence of $T_c(x)$ does not correlate with the $x(\text{Te})$ dependence of residual resistivity ratio, implying that the T_c increase found for $x(\text{Te}) > 0.3$ has an intrinsic origin.

Figure 2 shows the high-pressure phase diagrams of FeSe_{1-x}Te_x up to 8 GPa determined by the resistivity measurements performed by using the constant-load cubic anvil cell in Uwatoko group, ISSP, University of Tokyo. When Te composition $x(\text{Te})$ becomes larger than 0.1, the high-pressure magnetic order disappears, whereas the pressure-induced superconducting dome near the nematic end point is continuously found up to $x(\text{Te}) \approx 0.5$. In contrast to FeSe_{1-x}S_x, enhanced superconductivity in FeSe_{1-x}Te_x does not correlate with magnetism but with the suppression of nematicity. It is generally expected that the quantum fluctuations of electronic order are intensified near the end point of the associated order, so in the present case, nematic fluctuations are expected to be enlarged when the nematic order is suppressed with the Te substitution or pressure. Our results show that the superconducting dome exists near the end point of nematic order in FeSe_{1-x}Te_x, near which we have no magnetic order. These results highlight the paramount role of nonmagnetic nematic fluctuations for high-temperature superconductivity in this system.

References

- [1] See, for a review, T. Shibauchi, T. Hanaguri, and Y. Matsuda, *J. Phys. Soc. Jpn.* **89**, 102002 (2020).
- [2] K. Mukasa, K. Matsuura, M. Qiu, M. Saito, Y. Sugimura, K. Ishida, M. Otani, Y. Onishi, Y. Mizukami, K. Hashimoto, J. Gouchi, R. Kumai, Y. Uwatoko, and T. Shibauchi, *Nat. Commun.* **12**, 381 (2021).

Authors

K. Mukasa^a, K. Matsuura^a, M. Qiu^a, M. Saito^a, Y. Sugimura^a, K. Ishida^a, M. Otani^a, Y. Onishi^a, Y. Mizukami^a, K. Hashimoto^a, J. Gouchi, R. Kumai^b, Y. Uwatoko, and T. Shibauchi^a
^aThe University of Tokyo
^bKEK

PI of Joint-use project: T. Shibauchi
 Host lab: Uwatoko Group

Topological Spin Orders in a Centrosymmetric Tetragonal Magnet EuAl_4 Investigated by Polarized Neutron Scattering

Topologically nontrivial magnetic orders have been intensively investigated since the pioneering work on magnetic skyrmion lattice in MnSi , in which Dzyaloshinski-Moriya (DM) interactions arising from the chiral crystal structure and ferromagnetic interactions lead to long-period modulated magnetic orders including the skyrmion lattice state. Therefore, the early studies on magnetic skyrmions were focusing mainly on ferromagnetic systems with broken spatial inversion symmetry. However, a recent study on an itinerant triangular lattice magnet Gd_2PdSi_3 [1] has revealed that centrosymmetric system can host magnetic skyrmion lattice owing to frustration in magnetic interactions or coupling between local magnetic moments and conduction electrons. In fact, subsequent studies have found the emergence of skyrmion lattice states in centrosymmetric magnets.

In the present study, we have found that EuAl_4 , which is also a centrosymmetric magnet, exhibits two distinct skyrmion lattice states in magnetic field [2]. This system has a tetragonal crystal structure belonging to the space group of $I4/mmm$. By applying magnetic field along the c axis below 15 K, the system shows successive field-induced phase transitions, which is accompanied by anomalies in Hall resistivity. This is indicative of the topological Hall effect arising from a non-coplanar magnetic structure like skyrmion lattice state. To determine the magnetic structures in the field-induced phases, we performed polarized neutron scattering in a magnetic field at TAIKAN instrument (BL15) in the materials and life science experimental facility in J-PARC. By utilizing supermirror neutron spin polarizer and analyzer, we measured spin-flip and non-spin-flip scattering intensities of magnetic Bragg reflections appearing in the small-angle region in a magnetic field of 1 T with varying temperature. As a result, we found that this system exhibits rhombic and square lattices of Bloch-type magnetic skyrmion lattices in a magnetic field. We have further investigated magnetic phase transitions in zero magnetic field using the polarized triple-axis neutron spectrometer PONTA in JRR-3. The spectrometer was operated in the P_{zz} longitudinal polarization analysis mode, in which the polarization direction of the neutron

spins was set to be perpendicular to the horizontal scattering plane. Figure 1 shows the summary of the measurements at PONTA. We have identified four magnetic phases below 15 K in zero field. Phase I and V have the magnetic modulation wave vectors (q -vectors) of $(q,0,0)$, while phase IV does $(q,q,0)$. By analyzing the neutron spin polarization of the scattered neutrons, the low temperature phases (I and V) and the highest temperature phase (IV) are found to have screw-type and fan-type magnetic modulations, respectively. Interestingly, the intermediate phase, phase VI, has both $(q,0,0)$ and $(q,q,0)$ wave vectors. By assuming a multi- q magnetic order in this phase, a superposition of these wave vectors (and their counterparts $(0,q,0)$ and $(q,-q,0)$) results in another topologically-nontrivial magnetic order, which is distinct from the well-known magnetic skyrmion lattice state. We would also like to emphasize that the modulation periods of these incommensurate magnetic orders are relatively short, specifically, 2-3 nm, which cannot be resolved by Lorentz transmission electron microscope. The present study also demonstrates that polarized neutron scattering is quite useful to study short-period topological magnetic orders.

References

- [1] T. Kurumaji *et al.*, Science. **365**, 914 (2019).
- [2] R. Takagi *et al.*, Nat. Commun. **13**, 1472 (2022).

Authors

R. Takagi^a, N. Matsuyama^a, V. Ukleev^b, L. Yu^b, J. S. White^b, S. Francoual^c, J. R. L. Mardegan^c, S. Hayami^a, H. Saito, K. Kaneko^d, K. Ohishi^e, Y. Ōnuki^f, T. Arima^a, Y. Tokura^{a,g}, T. Nakajima, and S. Seki^a

^aThe University of Tokyo

^bPaul Scherrer Institute

^cDeutsches Elektronen Synchrotron (DESY)

^dJapan Atomic Energy Agency (JAEA)

^eComprehensive Research Organization for Science and Society (CROSS)

^fRIKEN-CEMS

PI of Joint-use project: R. Takagi

Host lab: Neutron Science Laboratory

High Field Quantum Phase in the Chromium Spinel Oxide HgCr_2O_4

The spin nematic state, which has long been discussed for magnets with frustrated interactions, is a spin analog of the nematic state in a liquid crystal. In this unconventional magnetic state, the fluctuations of spins, behaving like rod- or disk-shaped molecules, spontaneously select a preferred direction without conventional magnetic order. In this study, we have confirmed a possible spin nematic order in the chromium spinel oxide HgCr_2O_4 . This compound is known as a highly frustrated pyrochlore antiferromagnet with significant spin-lattice coupling. In fact, the wide half-magnetization plateau, which was stabilized by the lattice distortion, was reported in HgCr_2O_4 [1]. The magnetization process in the chromium spinel oxides has been accounted for the classical model with the bilinear and biquadratic interactions, derived by integrating out the lattice degrees of freedom [2]. However, the result of previous high field magnetization measurements indicated the existence of a phase, which cannot be explained by the classical model, just below the saturation field H_{c4} [3]. From the subsequent theory, this unknown phase was suggested to be the spin nematic phase, which is stabilized by the interplay of the spin-lattice coupling, geometrical spin frustration and quantum fluctuation [4]. To gain thermodynamic evidence for the existence

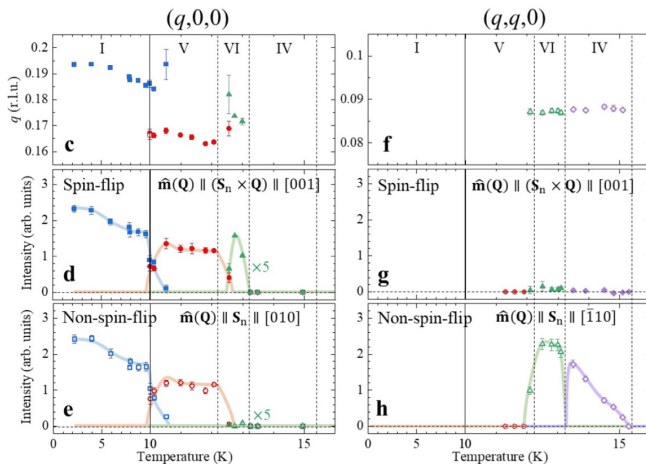


Fig. 1. Temperature dependence of spin-flip and non-spin-flip intensities of magnetic Bragg reflections in EuAl_4 measured by PONTA spectrometer in JRR-3.

of the magnetic ordering in the phase just below H_{c4} , we have performed the specific heat and the magnetocaloric effect measurements under pulsed high magnetic fields up to 42 T [5]. Figure 1 shows the results of the magnetocaloric effect measurements. The sharp dips at $H_{c3} \sim 37$ T and $H_{c4} \sim 40$ T in the magnetocaloric effect under the quasi-isothermal condition unambiguously exhibit the magnetic phase for $H_{c3} < H < H_{c4}$, whereas the fact that only a small kink is observed at H_{c3} under the quasiadiabatic condition indicates that the phase between H_{c3} and H_{c4} is gapless. From a peak of the specific heat at 38.5 K, we have also confirmed the ordering for $H_{c3} < H < H_{c4}$. From these thermodynamic measurements, we have obtained the magnetic field and temperature phase diagram, shown in Fig. 4. In the Heisenberg-type pyrochlore lattice magnet, the lowest-energy magnon states in a fully spin-polarized region above the saturation field are localized with flat dispersions owing to the geometrical configuration of the lattice. Therefore, the hopping of the single lowest-energy magnon is prohibited, thereby preventing kinetic energy gain. Meanwhile the spin-lattice coupling in HgCr_2O_4 brings the effective biquadratic interaction in Eq. (1). This biquadratic interaction contains a term $(S_i^-)^2(S_j^+)^2$, which induces hopping of a two-spin flipped state on a Cr^{3+} site to the nearest neighbor sites. Because of this hopping term, the two-magnon bound state

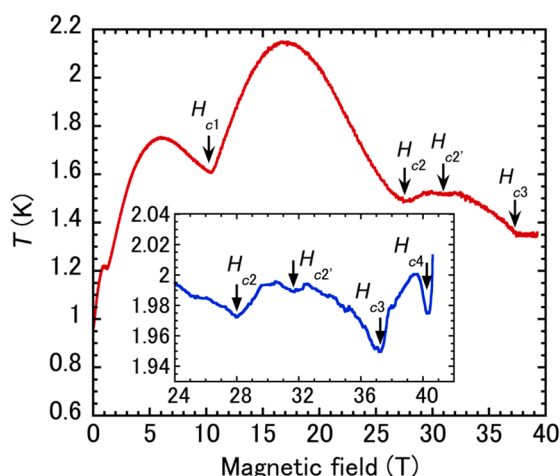


Fig. 1. Magnetocaloric effect of HgCr_2O_4 , observed under quasi-adiabatic condition. The inset shows that obtained under a quasi-isothermal condition.

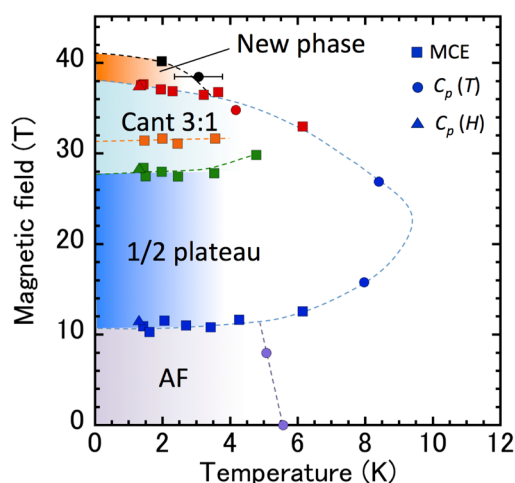


Fig. 2. Magnetic field and temperature phase diagram of HgCr_2O_4 , obtained from thermodynamic experiments. Squares, circles, and triangles are the transition points obtained from the magnetocaloric effect, temperature, and field dependencies of the specific heat, respectively. Dashed curves are drawn as guides for the eyes.

becomes stable and has a lower energy than two independent localized magnons in the fully polarized spin state. Decreasing the magnetic field in the fully polarized spin state causes softening of the two-magnon bound state. Then, the bound state touches to the ground state at the saturation field, resulting in its condensation, which leads to the spin nematic state. According to the calculation, the spin-component distribution, of which the projection to the plane perpendicular to the magnetic field has an ellipsoid shape, is aligned owing to the spin nematic order, thereby breaking the rotational symmetry around field. From our experimental results that suggest the existence of the gapless magnetic ordered phase between H_{c3} and H_{c4} , we consider that such a spin nematic order most probably appears in HgCr_2O_4 . The existence of an unknown magnetic phase just below the saturation was also reported for other chromium spinel oxides, CdCr_2O_4 and ZnCr_2O_4 from high-field experiments. It is possible that the appearance of the spin nematic phase is of universal nature in chromium spinel oxides.

References

- [1] H. Ueda, H. Mitamura, T. Goto, and Y. Ueda, *Phys. Rev. B* **73**, 094415 (2006).
- [2] K. Penc, N. Shannon, and H. Shiba, *Phys. Rev. Lett.* **93**, 197203 (2004).
- [3] S. Kimura, M. Hagiwara, T. Takeuchi, H. Yamaguchi, H. Ueda, Y. Ueda, and K. Kindo, *Phys. Rev. B* **83**, 214401 (2011).
- [4] E. Takata, T. Momoi, and M. Oshikawa, arXiv:1510.02373.
- [5] S. Kimura, S. Imajo, M. Gen, T. Momoi, M. Hagiwara, H. Ueda, and Y. Kohama, *Phys. Rev. B* **105**, L180405 (2022).

Authors

S. Kimura^a, S. Imajo, M. Gen, T. Momoi^b, M. Hagiwara^c, H. Ueda^d, and Y. Kohama

^aTohoku University

^bRIKEN

^cOsaka University

^dKyoto University

PI of Joint-use project: S. Kimura

Host lab: Kindo and Kohama Groups

A portable 77 Tesla Generator “PINK” for Novel Quantum Beam Experiments

The high magnetic field beyond 100 T is a promising tool to induce and uncover hidden or magnetic properties of materials thanks to its large Zeeman energy, that amounts to 134 K at 100 T for an electron spin of 1/2. However, experimentally, its usage is greatly regulated. First, the generation of B well above 100 T is principally difficult, being restricted to the destructive pulse magnets, where high magnetic fields last only a few μ -seconds, and a large explosion and electromagnetic noises accompany. Second, the experimental probe of material properties is limited. To overcome this situations, young researchers have made great effort for making possible to conduct electric resistivity, magnetization, ultrasound and magnetostriction measurements. Ikeda *et al.*, realized the magnetostriction measurement by using fiber Bragg grating technique and optical filter method, which is useful up to 1000 T range generated using electromagnetic flux compression method.

All these techniques are restricted to macroscopic measurements. In condensed matter physics, microscopic measurements and macroscopic ones complement with each other. Thus, microscopic measurements are in great demand. Recent single shot quantum beams like x-ray free electron laser (XFEL) [1] and femto-second Terahertz pulse

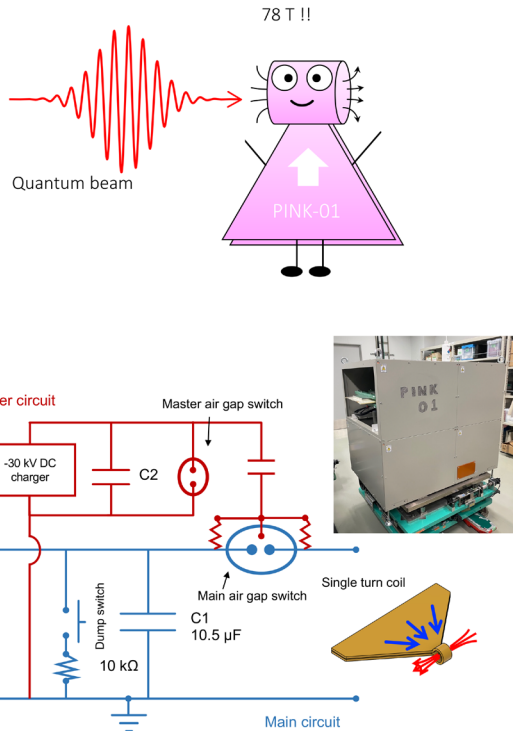
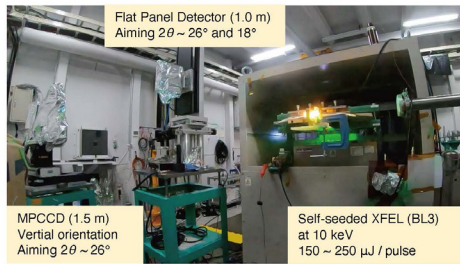
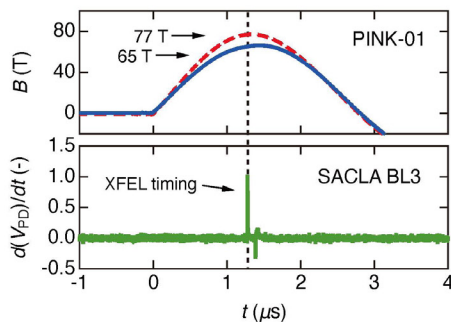


Fig. 1. Schematic image of PINK-01 and the electric circuit.

(a)



(b)



(c)

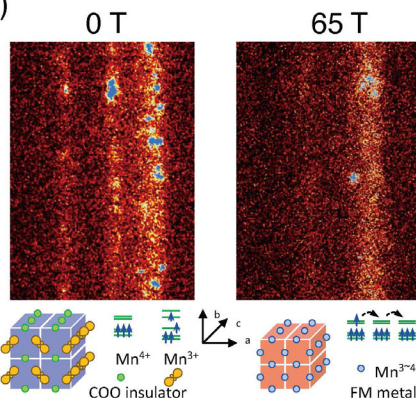


Fig. 2. (a) A photo, (b) synchronization between B pulse and XFEL pulse, and (c) a part of Debye-Scherrer ring of $\text{Bi}_{0.5}\text{Ca}_{0.5}\text{MnO}_3$ with and without magnetic field of 65 T.

techniques are in principle applicable for such purposes. However, the 100 T and 1000 T generators are built in a few large facilities. Besides, they are regularly occupied by daily experiments. For this reason, it is unable to move it to the x-ray facilities, or it is possible one to occupy the experimental site for developing new measurement only when the developing set-up is easily removable from the site.

This problem is solved if the ultrahigh magnetic field generator becomes portable. In the present study we have developed an ultrahigh magnetic field generator called PINK-01 (Portable INTense Kyokugenjiba with numbering 01). PINK-01 is shown to generate 77 T with a single turn coil with a 2.5 mm bore. We have carried PINK-01 to the XFEL facility SACLA in Japan. We have succeeded in obtaining XRD of powdered $\text{Bi}_{0.5}\text{Ca}_{0.5}\text{MnO}_3$ under 77 T where the charge ordered insulator phase is melted by the magnetic field inducing the forced ferromagnetic metallic phase. We clearly observe the lattice state change by the phase transition. We are now building new set up PINK-02 for 100 T generation and low temperature experiment with XFEL. Microscopic change of lattice will be uncovered in many kinds of materials at 100 T soon [2].

References

- [1] A. Ikeda, Y. H. Matsuda, X. Zhou, T. Yajima, Y. Kubota, K. Tono, and M. Yabashi, *Phys. Rev. Research* **2**, 043175 (2020).
- [2] A. Ikeda, Y. H. Matsuda, X. Zhou, S. Peng, Y. Ishii, T. Yajima, Y. Kubota, I. Inoue, Y. Inubishi, K. Tono, and M. Yabashi, *Appl. Phys. Lett.*, **120**, 142403 (2022).

Authors

A. Ikeda^a, Y. H. Matsuda, X. Zhou, S. Peng, Y. Ishii, T. Yajima, Y. Kubota^b, I. Inoue^b, Y. Inubishi^{b,c}, K. Tono^{b,c}, and M. Yabashi^{b,c}

^aUniversity of Electro-Communications

^bRIKEN SPring-8 Center

^cJapan Synchrotron Radiation Research Institute

PI of Joint-use project : A. Ikeda

Host lab : Y. H. Matsuda Group and X-ray Laboratory

Field-Induced Multiple Metal-Insulator Crossovers of Correlated Dirac Electrons of Perovskite CaIrO_3

The quantum phenomena of high-mobility relativistic electrons are issues of great interest in the modern condensed matter physics. So far, the quantum phenomena of relativistic electrons have been extensively studied in Dirac semimetals in which the electron correlation effect is small, but there is a growing interest in the quantum phenomena due to the strong electron correlations. One of fertile grounds to study this issue is the magnetically induced quantum limit (QL) in which the electrons are quasi-one-dimensionally

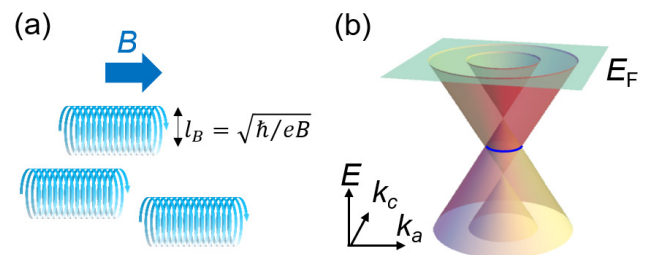


Fig. 1. (a) Quasi-one-dimensional confinement under high magnetic field in the quantum limit. (b) Schematic illustration of Dirac like dispersion near the line node.

(1D) confined under a sufficiently strong magnetic field B . In the QL, electrons in the lowest Landau level with the index $n = 0$ are confined in a scale of magnetic length $l_B = \sqrt{\hbar/eB}$ within a plane perpendicular to the magnetic field, while the momentum along the magnetic field is preserved (Fig. 1(a)). Previous theoretical studies proposed that nontrivial phases such as the axion charge density wave (CDW) and excitonic insulator can be induced, if the QL of the Dirac/Weyl electron can be realized in materials with the strong electron correlation [1]. However, the experimental realization of quantum limit in the strongly correlated electron material is a challenge and hence it has rarely been explored so far.

In this context, the correlated Dirac semimetal of perovskite CaIrO_3 provides an ideal arena to study the collective phenomena of high-mobility relativistic electrons in the QL. It has been proposed that the electron pocket emerging around U-point in the Brillouin zone of CaIrO_3 is caused by the Dirac band dispersion with a closed line-node protected by the nonsymmorphic crystalline symmetry ($Pbnm$), as illustrated in Fig. 1(b). Recently, it has been shown that the line node is precisely tuned close to E_F (~ 10 meV below E_F) and yields the Dirac electrons with dilute carrier density (less than $2 \times 10^{17} \text{ cm}^{-3}$) and high mobility exceeding $60,000 \text{ cm}^2\text{V}^{-1}\text{s}^{-1}$ due to strong electron correlations in the proximity to the Mott criticality [2]. As a result, the correlated Dirac electrons reach the QL at a modest magnetic field less than 10 T. However, the transport property in the QL of this material has not been explored so far, and a possibly striking feature of collective phenomena of the Dirac electrons remains elusive.

In this study, we have investigated the quantum limit transport of correlated Dirac electrons in the perovskite CaIrO_3 by means of magneto-transport measurements up to 55 T and theoretical calculations [3]. In the QL, the magnetoresistivity steeply increases around 10 T and the insulating state with a finite energy gap emerges around 18 T (Fig. 2). By further increasing the magnetic field, both the gap and resistivity dramatically decrease, resulting in the quasi-1D metallic state in the deep QL regime. The non-monotonic field dependence of the gap suggests that the field-induced insulating state originates from the collective electronic ordering, likely the charge density wave or spin density wave driven by the Fermi surface instability inherent to the quasi-one-dimensional $n = 0$ Landau levels with the

enhanced density of states under the magnetic field. The field-induced crossover between the metallic state and the gapped state appears in the fairly low magnetic field regime (10-30 T) among the conventional semimetals, highlighting the highly field-sensitive character of strongly correlated Dirac electrons relevant to the Mott criticality.

References

- [1] Z. Pan and R. Shindo, Phys. Rev. B **100**, 165124 (2019).
- [2] J. Fujioka, R. Yamada, M. Kawamura, S. Sakai, M. Hirayama, R. Arita, T. Okawa, D. Hashizume, M. Hoshino, and Y. Tokura, Nat. Commun. **10**, 362 (2019).
- [3] R. Yamada, J. Fujioka, M. Kawamura, S. Sakai, M. Hirayama, R. Arita, T. Okawa, D. Hashizume, T. Sato, F. Kagawa, R. Kurihara, M. Tokunaga, and Y. Tokura, npj Quantum Mater. **7**, 13 (2022).

Authors

R. Yamada^a, J. Fujioka^b, M. Kawamura^c, S. Sakai^c, M. Hirayama^{a,c}, R. Arita^{a,c}, T. Okawa^a, D. Hashizume^c, T. Sato^c, F. Kagawa^{a,c}, R. Kurihara, M. Tokunaga, and Y. Tokura^{a,c}

^aThe University of Tokyo

^bTsukuba University

^cCEMS RIKEN

PI of Joint-use project: J. Fujioka

Host lab: Tokunaga Group

NMR Relaxation Time Measurements in Pulsed Field

Interesting electronic states are frequently found in magnetic fields, where magnetic interactions inherent in material compete with magnetic energy provided by the external magnetic fields. To cause significant impact on the electronic state, extremely high magnetic fields generated by the pulsed-field technology should be applied to the material. The recent advances in pulsed-field technology allow us to access novel field-induced quantum states by its ability to generate extreme magnetic fields. However, various experiments in pulsed field have been a challenge because of the short duration of field generation time. In this work, we incorporate a versatile NMR spectrometer with the dynamically controlled pulsed field to perform NMR measurement in pulsed field and demonstrate the nuclear spin-lattice and spin-spin relaxation rate measurements.

NMR experiment in pulsed field was difficult because the resonant frequency determined by the external field strength continuously and rapidly changes following the pulsed-field profile. Previously the field-sweep NMR spectrum has been obtained by quickly recording the NMR intensity during the rapid variation of field strength [1,2]. To achieve a sufficiently long measurement time, which is determined by the total pulse width, a large-scale electromagnet with a long time duration of typically ~ 100 ms has been used for the NMR experiment. In contrast, we combined our NMR spectrometer with the “flat-top” pulsed field; a novel type of pulsed field realized by controlling the pulsed-field strength dynamically [3]. Since the field drift can be suppressed to less than 100 ppm during when the pulsed field is under the feedback control, we can perform any conventional NMR measurements developed for the steady fields even in a rather short time duration of ~ 30 ms. Since a smaller energy is required to generate a shorter pulsed field, this development facilitates the pulsed-field NMR experiment in any kinds of pulse magnets, such as a portable pulsed-field generator installed in a small laboratory.

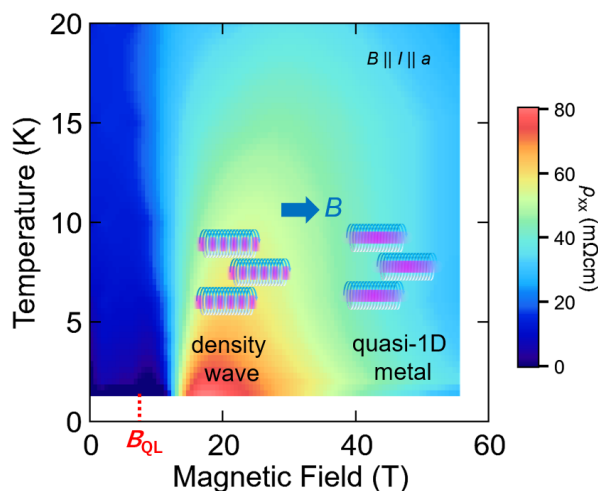


Fig. 2. The contour plot of resistivity as a function of temperature and magnetic field. The density wave and quasi-one-dimensional metallic phase may appear in the quantum limit of Dirac electrons around the line node.

The most important advantage of the flat-top pulse is that the relaxation of physical quantities can be traced during the quasi-steady field state. With this feature, we can perform the nuclear spin-lattice relaxation time T_1 measurement with conventional saturation-recovery method, which was believed to be impossible in pulsed field. In addition to the quasi-steady condition of the magnetic fields, we need high reproducibility of field strength to obtain the relaxation profile of the nuclear magnetization. As the spin-echo pulses to observe NMR signal disturb the nuclear spin states, we need to repeat several NMR measurements with various delays between the saturation and the spin-echo pulses at independent pulsed fields. We confirmed the reproducibility of field strength and the NMR intensity by repeating 10 independent field pulses and by measuring ^{65}Cu -NMR signal with the same condition at each pulse [4]. Encouraged by the high reproducibility of flat-top pulse we performed the T_1 measurement for a metallic antiferromagnet CrB_2 , and the obtained relaxation profile is shown in Fig.1(a) as the filled symbols. The open symbols are the result obtained at the same field in a real-steady condition. The agreement between the results in pulse and steady fields manifests the feasibility of relaxation time measurement in pulsed fields. However, as the total pulse duration was ~ 30 ms for the pulse magnet used in the current study, the accessible time scale of T_1 is limited up to ~ 4 ms which is usually too short to achieve the thermal equilibrium state. To solve this issue, we are now working to implement the NMR spectrometer to a larger pulse magnet with longer pulse duration, which will allow us to extend the accessible time scale of T_1 . We also successfully performed the nuclear spin-spin relaxation time T_2 measurement with the same setup [5]. As the typical times-

cale for T_2 is shorter than 1 ms, T_2 measurement is more suitable for pulsed fields. Figure 1 (b) shows the T_2 decay profiles obtained in the pulsed field (filled) and steady field (open). The consistent results again confirm the feasibility of T_2 measurement in pulsed fields.

Besides the T_1 and T_2 measurements, combination of versatile NMR spectrometer and flat-top pulse enables the frequency-sweep NMR spectrum measurement and the constant-rate field-sweep NMR spectrum measurement. [4,5] With these developments, microscopic magnetism in materials can be unveiled up to very high magnetic fields. So far, microscopic experiment that can be performed at such high magnetic field is still limited. Our pulsed-field NMR technique developed here will provide crucial information to understand the field-induced quantum states.

References

- [1] J. Kohlrautz, J. Haase, E. L. Green, Z. T. Zhang, J. Wosnitza, T. Herrmannsdörfer, H. A. Dabkowska, B. D. Gaulin, R. Stern, and H. Kühne, *J. Magn. Reson.* **271**, 52 (2016).
- [2] A. Orlova, E. L. Green, J. M. Law, D. I. Gorbunov, G. Chanda, S. Krämer, M. Horvatić, R. K. Kremer, J. Wosnitza, and G. L. J. A. Rikken, *Phys. Rev. Lett.* **118**, 247201 (2017).
- [3] Y. Kohama and K. Kindo, *Rev. Sci. Instrum.* **86**, 104701 (2015).
- [4] Y. Ihara, K. Hayashi, T. Kanda, K. Matsui, K. Kindo, and Y. Kohama, *Rev. Sci. Instrum.* **92**, 114709 (2021).
- [5] Y. Kohama, T. Nomura, S. Zherlitsyn, and Y. Ihara, submitted to *J. Appl. Phys.*

Authors

Y. Ihara^a, K. Hayashi^a, T. Kanda, K. Matsui, K. Kindo, and Y. Kohama^a
^aHokkaido University

PI of Joint-use project: Y. Ihara
 Host lab: Kindo and Kohama Groups

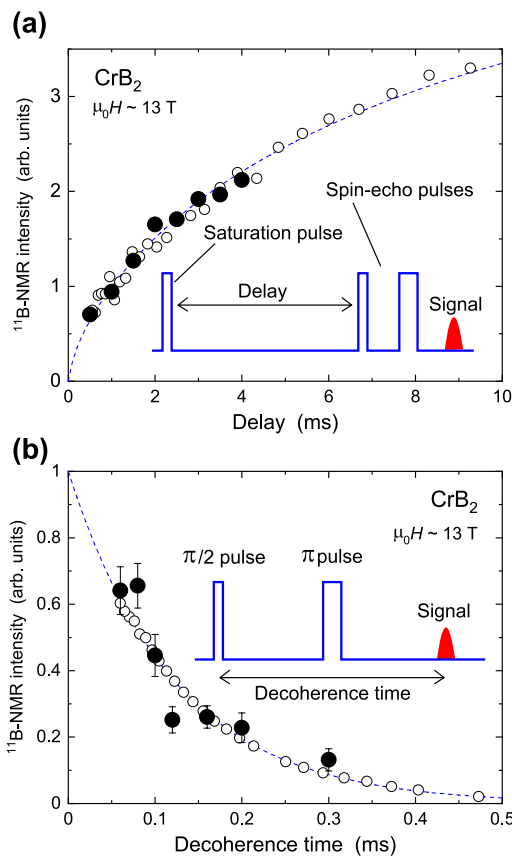


Fig. 1. Recovery (a) and decay (b) profiles of nuclear magnetization measured for a metallic antiferromagnet CrB_2 . The filled (open) symbols are the data obtained in pulsed (steady) fields. Consistent results in both cases confirm the feasibility of relaxation measurement in flat-top pulse. Insets are the sketches of the NMR pulse sequences used for corresponding measurements.

Time-Resolved X-Ray Photoelectron Diffraction Using an Angle-Resolved Time-of-Flight Electron Analyzer

Photoelectron spectroscopy (PES) is a powerful experimental approach for investigating chemical composition, electronic states, and atomic structure of a material. Recently, the PES measurement method is conducted with temporal resolutions and the experiment becomes a successful method to track these quantities during the dynamical events of a sample. At SPring-8 BL07LSU, such a time-resolved PES technique is developed and the beamline endstation has been opened for users. In the present research, we combined it with angular resolution and demonstrated a time-resolved experiment of X-ray photoelectron diffraction (XPD) [1].

The time-resolved measurements were performed by a pump-probe method that combined synchrotron radiation (SPring-8 BL07LSU) and laser (BL07LASER) pulses [2,3]. Photon energy of synchrotron radiation was set at $h\nu = 300\text{eV}$, while that of laser at $h\nu = 1.55\text{eV}$. Angle-resolved spectra were obtained with a two-dimensionally angle-resolved time-of-flight (2DARTOF) analyzer [3]. The photoelectrons, detected by the 2D delay line detector, were recorded at the arrival time (t) and position (x, y), subsequently converted into energy (E) and 2D emission angle (θ_x, θ_y). A demonstration experiment was made on a silicene layer, a honeycomb lattice of Si atoms, on a ZrB_2 substrate. Figures 1 (a) and 1 (b) show the Si 2p XPD patterns of two atomic sites, α and β , in the silicene. The two sites appear at different binding energies of PES, as shown in Fig. 1 (c). One can find in Fig.1 (a,b) that the experimental XPD pattern

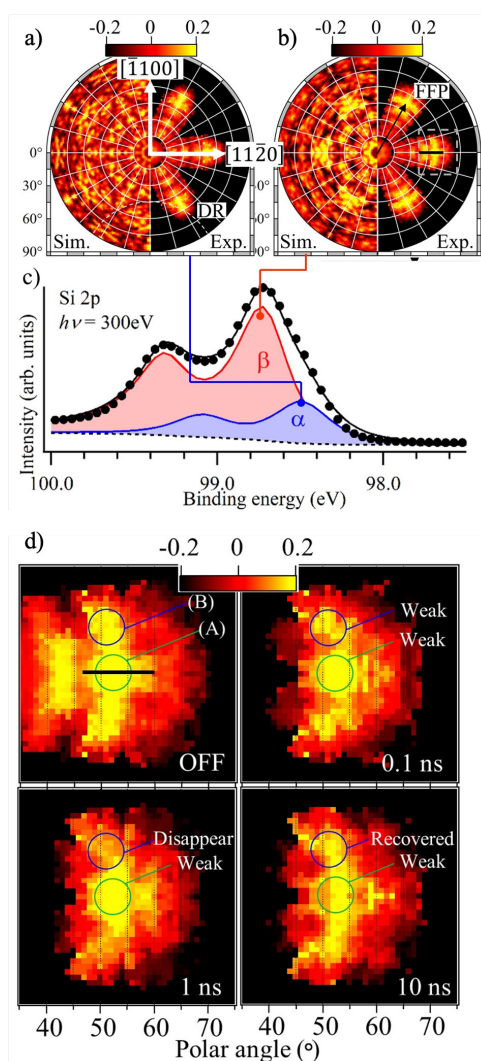


Fig. 1. (a,b) XPD patterns of the Si 2p core levels at the α and β sites in (c) XPS spectrum. (d) Time-resolved XPS pattern of the β site taken at various delay times [1].

is reproduced by the simulation. Focusing on the pattern at the β site, the temporal variation can be detected after the delay time. As presented in Fig. 1(d), the features, labeled A and B, shows temporal changes, weakening, disappearance, and recovery, during sub-nanoseconds (ns) to 10 ns. These results indicate that the time-resolved XPD experiment can be effectively made with a 2DARTOF analyzer. The novel approach is useful to examine the structural changes during dynamical events, such as photocatalysis and photo-induced phase transition.

References

- [1] A. K. Ang, Y. Fukatsu, K. Kimura, Y. Yamamoto, T. Yonezawa, H. Nitta, A. Fleurence, S. Yamamoto, I. Matsuda, Y. Yamada-Takamura, and K. Hayashi, *Jpn. J. Appl. Phys.* **59**, 100902 (2020).
- [2] J. Miyawaki, S. Yamamoto, Y. Hirata, M. Horio, Y. Harada, and I. Matsuda, *AAPPS Bulletin* **31**, 25 (2021).
- [3] M. Ogawa *et al.*, *Rev. Sci. Instrum.* **83**, 023109 (2012).

Authors

K. Hayashi^a and I. Matsuda
^aNagoya Institute of Technology

PI of Joint-use project: K. Hayashi
 Host lab: I. Matsuda Group

